

Building intuition of iron evolution during solar cell processing through analysis of different process models

Ashley E. Morishige¹ · Hannu S. Laine² · Jonas Schön³ · Antti Haarahiltunen² · Jasmin Hofstetter¹ · Carlos del Cañizo⁴ · Martin C. Schubert³ · Hele Savin² · Tonio Buonassisi¹

Received: 23 April 2015 / Accepted: 22 June 2015 / Published online: 14 July 2015
© Springer-Verlag Berlin Heidelberg 2015

Abstract An important aspect of Process Simulators for photovoltaics is prediction of defect evolution during device fabrication. Over the last twenty years, these tools have accelerated process optimization, and several Process Simulators for iron, a ubiquitous and deleterious impurity in silicon, have been developed. The diversity of these tools can make it difficult to build intuition about the physics governing iron behavior during processing. Thus, in one unified software environment and using self-consistent terminology, we combine and describe three of these Simulators. We vary structural defect distribution and iron precipitation equations to create eight distinct Models, which we then use to simulate different stages of processing. We find that the structural defect distribution influences the final interstitial iron concentration ($[Fe_i]$) more strongly than the iron precipitation equations. We identify two regimes of iron behavior: (1) *diffusivity-limited*, in which iron evolution is kinetically limited and bulk $[Fe_i]$ predictions can vary by an order of magnitude or

more, and (2) *solubility-limited*, in which iron evolution is near thermodynamic equilibrium and the Models yield similar results. This rigorous analysis provides new intuition that can inform Process Simulation, material, and process development, and it enables scientists and engineers to choose an appropriate level of Model complexity based on wafer type and quality, processing conditions, and available computation time.

1 Introduction

Technical computer-aided design has accelerated optimization of semiconductor design and processing for the last few decades. Photovoltaic (PV) device simulators, which compute device performance on the basis of material properties and geometry inputs, are mature and ubiquitous in industry [1–6]. In contrast, Process Simulations are less developed. An important use of Process Simulators is to simulate the evolution of performance-limiting bulk defects in response to varying time-temperature profiles and wafer-surface conditions. As PV devices become increasingly bulk-limited [7], as new wafer materials are developed, and as PV manufacturing becomes even more cost competitive, there is an increasing need for accurate and fast Process Simulations to maximize the potential of each substrate.

A common focus of defect-related Process Simulators is iron, one of the most ubiquitous, detrimental [8], and easily detected [9, 10] impurities in *p*-type PV-grade silicon. Iron can take different forms in silicon: point defects (including interstitials, interstitial–acceptor pairs, and substitutional atoms), iron-silicide precipitates (including the similar α - and β -phase precipitates, and early-stage γ -phase platelets),

Electronic supplementary material The online version of this article (doi:10.1007/s00339-015-9317-7) contains supplementary material, which is available to authorized users.

✉ Ashley E. Morishige
aemorish@alum.mit.edu; buonassisi@mit.edu

¹ Department of Mechanical Engineering, Massachusetts Institute of Technology, Cambridge, MA 02139, USA

² Department of Micro- and Nanosciences, Aalto University, 02150 Espoo, Finland

³ Characterization of Process Materials and Silicon Materials, Fraunhofer Institute for Solar Energy Systems, 79100 Freiburg, Germany

⁴ Instituto de Energía Solar, Universidad Politécnica de Madrid, 28040 Madrid, Spain

and inclusions. Interstitial iron and β -phase precipitates are the most relevant for crystalline silicon photovoltaics. See [8, 11–15] for further detail. The chemical state and distribution of iron impurities evolve during high-temperature solar cell processing steps [8, 16–19] because of the exponential dependence of iron point defect solubility and diffusivity on temperature. As the different states of iron exert varying impacts on minority carrier lifetime [20], accurate modeling of iron evolution is critical to determining its impact on the finished device.

At least eight research groups have developed tools to simulate the evolution of iron during solar cell processing [21–28]. These Simulators differ in two significant ways: (1) physics: they make different assumptions regarding the governing physics of nucleation, precipitation, growth, and dissolution of iron-silicide precipitates, and (2) implementation: they use different coding environments, with unique mesh assumptions and numerical solvers. Most Simulators have been validated by experimental results, for different processing conditions and input wafer impurity types and concentrations [25–27]. Because of differences in coding and validation, it can be difficult for a third party to compare models and determine the most relevant underlying physics for a wider range of industrially relevant processing and material conditions.

In this study, we combine into one coding environment the salient features of iron Process Simulators developed at Aalto University [25], Fraunhofer Institute for Solar Energy Systems [26], and Massachusetts Institute of Technology jointly with Universidad Politécnica de Madrid [27]. Our goals are: (1) to elucidate the essential physics at each process step, (2) to determine the necessary Model complexity to accurately simulate today's materials and processes, and (3) to guide future materials, device, and Process Simulation development by building intuition for the behavior of iron.

The intuition developed here for iron in p -type Si can be generalized to other metal metal impurities and to n -type Si. We evaluate ingot crystallization, thermal annealing, phosphorus diffusion, and contact metallization firing. We systematically vary structural defect distribution and iron precipitation equations to create eight distinct Models, which we describe in detail with self-consistent terminology and with emphasis on the aspects that are most important for iron evolution. As simulation outputs, we report the concentration of interstitial iron ($[Fe_i]$), the state with the greatest lifetime impact on p -type silicon [29–31]. We also report iron-silicide precipitate spatial density and size, as precipitates have a secondary lifetime impact [12, 13, 20] and they may be the more dominant recombination center in n -type silicon [31–38].

Notably, we identify two regimes of iron behavior, and we describe how they map onto the different Models,

process conditions, and crystalline silicon wafer materials of varying type and quality:

(1) *Diffusivity-limited* When the availability of heterogeneous nucleation sites is low, iron diffusion to precipitation sites limits precipitation. In this regime, physical assumptions regarding bulk-iron transport and precipitate nucleation can lead to variations of simulated residual interstitial iron point defect concentrations up to an order of magnitude. This condition describes processing steps during which the annealing temperature is insufficient to dissolve all iron-silicide precipitates and iron gettering is kinetically limited.

(2) *Solubility-limited* In this regime, the iron point defect concentration is governed primarily by either bulk solubility, precipitate dissolution, or segregation to the emitter, which is governed by the difference between the solubility in the bulk and in the emitter. Variation between different Models tends to be small. This condition describes iron contamination levels either close to the solid solubility at the annealing temperature (e.g., the early stages of crystallization) or below the solid solubility when there is a high density of precipitation sites or strong segregation to the emitter occurs. In this regime, iron behavior can be considered at or near thermodynamic equilibrium.

2 Model descriptions

We employ the following definitions consistently throughout our manuscript. Because these definitions are not universal, we capitalize them.

Simulator A computer-based software tool designed to complement and accelerate trial-and-error experimentation.

Process Simulation A Simulation that is carried out by a Simulator which is designed to predict defect evolution during solar cell processing, in response to varying time-temperature profiles and surface chemistry.

Model The set of physics-based assumptions that drive the Simulation. In Process Simulations, the Model consists of coupled kinetic and thermodynamic equations, with both geometric and chemical boundary conditions.

Model Element One of the physics-based assumptions coupled into the Simulation. Model Elements include, among others, the definition of the structural defect distributions (grain boundaries, dislocations) and the equations governing precipitation behavior (Ham's law [39], Fokker–Planck equation (FPE) [25]).

2.1 Systematic variation of model elements

To determine the Model Elements with greatest impact on predicted final iron distribution, we explore four variations of precipitation site distribution (see Sect. 2.2) and two

iron precipitation equations (see Sect. 2.3), resulting in a 4×2 matrix of eight unique Models (Fig. 1). This selection of Model Elements is informed by industrial relevance and the nearly decade-long experience of iron simulation at each institution. With these eight Models, we simulate the entire silicon solar cell processing sequence, with associated time-temperature profiles and changing boundary conditions (e.g., the presence or absence of phosphorus in-diffusion).

The following parameters are invariant among the eight Models: The crystal grain is 3 mm wide, the wafer is 180 μm thick, and the boron doping concentration is $3 \times 10^{16} \text{ cm}^{-3}$. We simulate phosphorus in-diffusion and gettering from both wafer surfaces. The local iron solid solubility in silicon, C_s , is provided by Aoki et al. [40]. Although strain in the silicon lattice at structural defects can enhance the solid solubility of iron [26, 41], we neglect this enhancement because it has only a minor effect on the iron distribution. Additionally, most of the solar cell processes that we simulate occur at higher temperatures where this solubility enhancement becomes negligible. The solubility and concentration gradient diffusion equations are solved by the algorithm suggested by Hieslmair et al. [42], and the diffusivity of iron, D_{Fe} , is described by Istratov et al. [11, 43]. Phosphorus diffusion is simulated as described in Bentzen et al. [44]. The phosphorus diffusion gettering model (i.e., the diffusion-segregation equation) was taken from Tan et al. [45, 46], and the iron segregation coefficient as a function of phosphorus doping concentration is taken from Haarahiltunen et al. [47]. During heating, we assume a negligible precipitate dissolution energy barrier in all models—precipitates can start to dissolve the

instant the solid solubility exceeds $[\text{Fe}_i]$ [26, 48]. Lastly, we assume that structural defects are stationary and neither generated nor annihilated by processing, as the used temperature ranges are not high enough to allow significant dislocation movement [49–51].

2.2 Four structural defect distributions

In this section, we describe the four variations of precipitation sites used in our eight Models (Fig. 1). Precipitation sites are locations along structural defects where precipitates can, but are not required to, nucleate. The number of precipitation sites is the maximum number of precipitates allowed. While the density and distribution of precipitation sites can be varied, their nature cannot: All nucleation sites are modeled as sites along dislocations and precipitation is equally favorable at each site. See “Appendix 1” for more details.

The simplest precipitation site (defect) distribution is a homogeneous distribution. This is equivalent to a wafer with a constant dislocation density and no grain boundaries. This precipitation site distribution has the lowest computational complexity: Without the presence of the phosphorus layer, only relaxation gettering, i.e., the nucleation and precipitation of impurities driven by supersaturation during cooling, occurs, and it proceeds similarly in every point of the wafer. Thus, only a single simulation point is needed to fully account for the changes in the iron distribution and chemical state. If a phosphorus layer is present on either surface of the wafer, segregation gettering causes changes in the iron distribution along the wafer depth, requiring a 1D finite-element simulation. This homogeneous defect distribution is referred to as “0D/1D.”

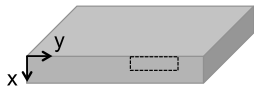
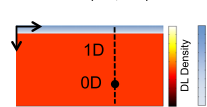
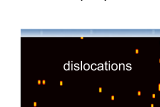
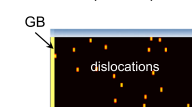

Wafer Cross-Section								
Structural Defect Distribution	Homogeneous (0D/1D)		2D Dislocations (DL)		2D Dislocations + Grain Boundary (DL+GB)		2D Grain Boundary (GB)	
								
Precipitate Distribution at Defects	Fokker-Planck	Ham's Law	Fokker-Planck	Ham's Law	Fokker-Planck	Ham's Law	Fokker-Planck	Ham's Law
Model Name	0D/1D FPE	0D/1D Ham	2D FPE DL	2D Ham DL	2D FPE DL + GB	2D Ham DL + GB	2D FPE GB	2D Ham GB

Fig. 1 Summary of the eight Models. *First row* Crystalline silicon wafer cross-section schematic with simulation domain outlined. *Second row* Schematics of the four structural defect distributions: a 0D/1D homogeneous distribution and three 2D heterogeneous distributions, including only dislocations (DL), dislocations and a grain boundary (DL+GB), and only a grain boundary (GB). The DL

density colorbar is a log scale with range $0\text{--}2 \times 10^8 \text{ cm}^{-2}$. The phosphorus colorbar is a qualitative illustration. *Third row* For each structural defect distribution, two sets of precipitation equations are analyzed, including Fokker–Planck equation and Ham’s law. Precipitation occurs at the structural defects. *Fourth row* The shorthand Model names used in the rest of the paper

To account for heterogeneous precipitation site distributions, we add a second dimension to our Models. The first 2D Model consists of heterogeneously distributed dislocations and no grain boundaries, representing mono-like [52–59] and epitaxial silicon [60–63]. The second 2D Model adds a grain boundary to the dislocations, simulating conventional multicrystalline silicon (mc-Si). The grain boundary is modeled as a dense network of dislocations. The third 2D Model comprises a grain boundary but no dislocations representing regions of high-performance mc-Si [64] or ribbon growth on silicon (RGS) material [65, 66], where the relative effect of the intra-grain regions is small relative to the effect of the grain boundaries. These 2D Models are referred to as the “2D DL”, “2D DL+GB”, and “2D GB”, respectively. Further details are in “Appendix 1”.

2.3 Two sets of iron precipitation equations

For the Model Element to describe iron-silicide precipitate formation, either of two sets of equations can be used: one based on Ham’s law [39], and the other using the FPE [25]. A rigorous mathematical description of both appears in “Appendix 2.” Here, we provide qualitative descriptions that are sufficiently detailed to infer differences between resulting iron distributions in subsequent sections.

Iron supersaturation is the driving force for precipitation in both sets of equations. Thus, to initiate precipitation of interstitial iron, the dissolved concentration must be sufficiently greater than the equilibrium solid solubility (i.e., typically, the wafer must be cooling down).

Ham’s law assumes a density of precipitation sites that does not vary over time, with all precipitates modeled as spheres. Mathematically, at each grid point, this is equivalent to the precipitate density being constant and the precipitate size distribution being a time-dependent delta function. Precipitate growth begins the instant iron supersaturation is achieved. This simplicity makes Ham’s law computationally straightforward, yet there are certain disadvantages. The precipitate size delta function means that Ostwald ripening (i.e., the dissolution of small precipitates to favor the growth of large ones) cannot be modeled. The constant precipitate density implies that complete precipitate dissolution is not accurately modeled. Precipitate nucleation is also not simulated with Ham’s law. For these two reasons, crystallization is not simulated with the Ham’s law precipitation Model. For process steps after crystallization, including phosphorus diffusion gettering, the average density of precipitates used in Ham’s law is calculated from the results of the FPE-based simulation of ingot crystallization.

The FPE Model Element describes precipitate size at each grid point by a distribution function, not a delta

function. The time evolution of the distribution is governed by the FPE. Consequently, the precipitate density is time varying, although the precipitation site density is constant (i.e., structural defect concentration is invariant). This set of equations, while computationally complex relative to Ham’s law, can describe three important phenomena: (1) explicit inclusion of a precipitation site capture radius and a precipitation nucleation barrier allows for simulation of precipitate nucleation, (2) the Ostwald ripening effect mentioned above, and (3) how faster cooling from high temperature leads to higher densities of smaller precipitates (and vice versa).

It is important to highlight two subtle points about our implementation of the FPE: First, precipitation does not commence instantaneously with iron supersaturation upon cooling. For a precipitate to nucleate, its radius must be greater than the critical radius determined by the Gibbs free energy. Second, we assume spherical precipitates for Ham’s law and platelets for the FPE Model Element. Precipitate growth depends on the degree of iron point defect supersaturation and on iron point defect capture, which depends on the precipitate radius. The precipitate growth rate for FPE is higher than that for Ham’s law, because the capture radius of platelets (FPE) depends on $n^{1/2}$ (where n is number of iron atoms per precipitate) while that of spheres (Ham’s law) depends on $n^{1/3}$.

Both points are visible in Fig. 2, which shows an example of the net precipitate growth rates for both Models (see “Appendix 2”) as a function of precipitate size. The effect of the differences in precipitate growth mechanisms of the two precipitation models can be summarized by

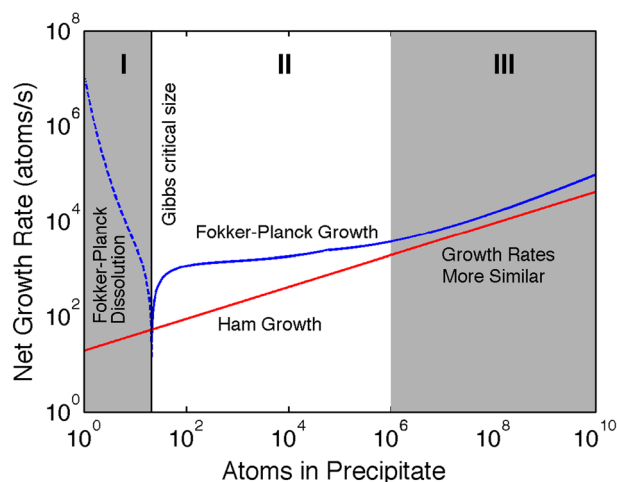


Fig. 2 Net precipitate growth rate as a function of precipitate size for Ham’s law (red) and Fokker–Planck equation (blue), for a given annealing temperature (815 °C) and total iron concentration (10¹⁴ cm^{−3}). Stages I, II, and III of precipitate growth are delineated. The dashed blue line indicates negative growth (i.e., dissolution)

comparing the two rates. Figure 2 highlights three stages of iron precipitation. Although the x - and y -axis values depend on precise dissolved iron concentration and temperature, these stages are general. In Stage I, when the degree of iron supersaturation is small, precipitates will grow in Ham's law but not in FPE (blue dashed line indicates negative total growth rate) because below the Gibbs critical size, precipitates are unstable and tend to dissolve. In Stage II, the Gibbs free energy is favorable for precipitate formation in FPE, leading to explosive precipitate growth at the onset of Stage II. In Stage III, the growth rate of precipitates depends on iron capture, and the subtlety of the $n^{1/2}$ versus $n^{1/3}$ dependence can be observed.

3 Simulated solar cell fabrication processes

To illustrate the governing physics and to elucidate similarities and differences between the Models during realistic processing conditions, all high-temperature steps during the solar cell fabrication process are simulated, from crystal growth to contact metallization firing. Crystal growth starts from the melting temperature of silicon, when metals are dissolved, and often involves slow temperature ramps (for ingot materials, which comprise 90 % of the solar market). During crystal growth, the governing physics is relaxation gettering. In contrast, all other device fabrication steps involve relatively lower temperatures (often resulting in iron solid solubilities below the total iron concentration), relatively faster temperature ramps, and the presence of a phosphorus-rich surface boundary layer. The governing physics includes both relaxation and segregation gettering, the latter of which is responsible for redistributing metals on the basis of solubility differences between the bulk and the phosphorus-rich boundary layer. For each process step, we apply the framework of the *solubility*- and *diffusivity*-limited regimes introduced in Sect. 1.

3.1 Crystallization and re-heating: processes without a phosphorus-rich boundary layer

3.1.1 Crystallization

The solar cell process begins with crystallization (ingot solidification), the step that defines as-grown wafer properties. Crystal cooling starts with fully dissolved iron, and as cooling proceeds, the interstitial iron concentration decreases and the precipitated iron concentration increases. As discussed in Sect. 2.3, crystallization is simulated only with the FPE-based Models. The crystallization cooling rate is a key parameter for controlling post-crystallization $[\text{Fe}_i]$ [25]. For the time-temperature profile, we assume a

linear cooling from 1200 to 200 °C at 1.35 °C/min. We consider typical mc-Si initial total iron concentrations of $[\text{Fe}_0] = 3.5 \times 10^{13} \text{ cm}^{-3}$ and $2 \times 10^{14} \text{ cm}^{-3}$ both for industrial relevance and consistency with previous work [67].

The spatially resolved precipitation site densities and the interstitial iron distributions after crystal cooling are shown in Fig. 3 for the 2D defect distributions with the lower contamination level of $[\text{Fe}_0] = 3.5 \times 10^{13} \text{ cm}^{-3}$. A strong correlation is seen between precipitation site density and low $[\text{Fe}_i]$ because Fe_i internally getters to and precipitates at the structural defects as the silicon cools during crystallization. In all Models, regions of higher structural defect density and thus nucleation site density contain more precipitated iron after crystallization, as observed experimentally [15, 68, 69]. During subsequent processing steps, precipitated iron can reduce device performance because precipitates can limit the lifetime [20] and dissolving precipitates release Fe_i into the bulk [69–71].

To understand how the iron distribution evolves during crystallization, we plot the temperature, solubility, and iron distribution as a function of time for the four Models for the higher $[\text{Fe}_0] = 2 \times 10^{14} \text{ cm}^{-3}$ (Fig. 4). See Online Resource 1 for the evolution of temperature, solubility, and diffusivity as function of time during the crystallization. Results for both $[\text{Fe}_0]$ are in Online Resource 2. For all Models, a monotonic reduction in $[\text{Fe}_i]$ is observed. $[\text{Fe}_i]$ is reduced by nucleation of new precipitates and growth of existing ones. At the beginning of crystallization,

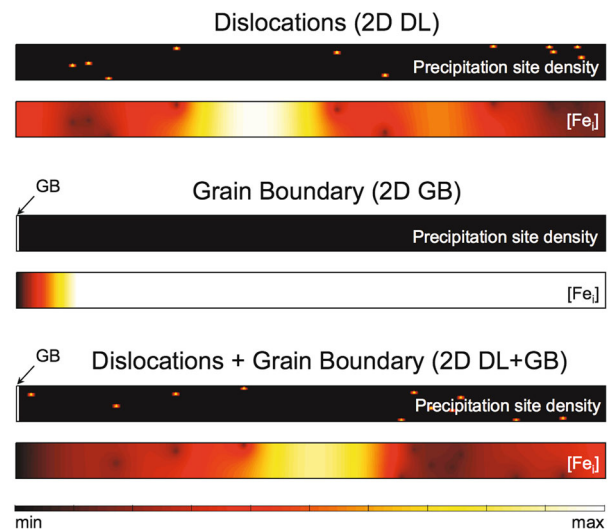


Fig. 3 Post-crystallization spatially resolved precipitation site density and $[\text{Fe}_i]$ generated from input parameters for the 2D Models: DL, GB, and DL+GB with $[\text{Fe}_0] = 3.5 \times 10^{13} \text{ cm}^{-3}$. Color scale is linear with precipitation site density range $0\text{--}5 \times 10^{11} \text{ cm}^{-3}$ and $[\text{Fe}_i]$ range $0\text{--}10^{13} \text{ cm}^{-3}$. Only the Fokker–Planck precipitation equation is used. Precipitation site density and $[\text{Fe}_i]$ are inversely correlated because $[\text{Fe}_i]$ is internally gettering to precipitation sites during ingot cooling

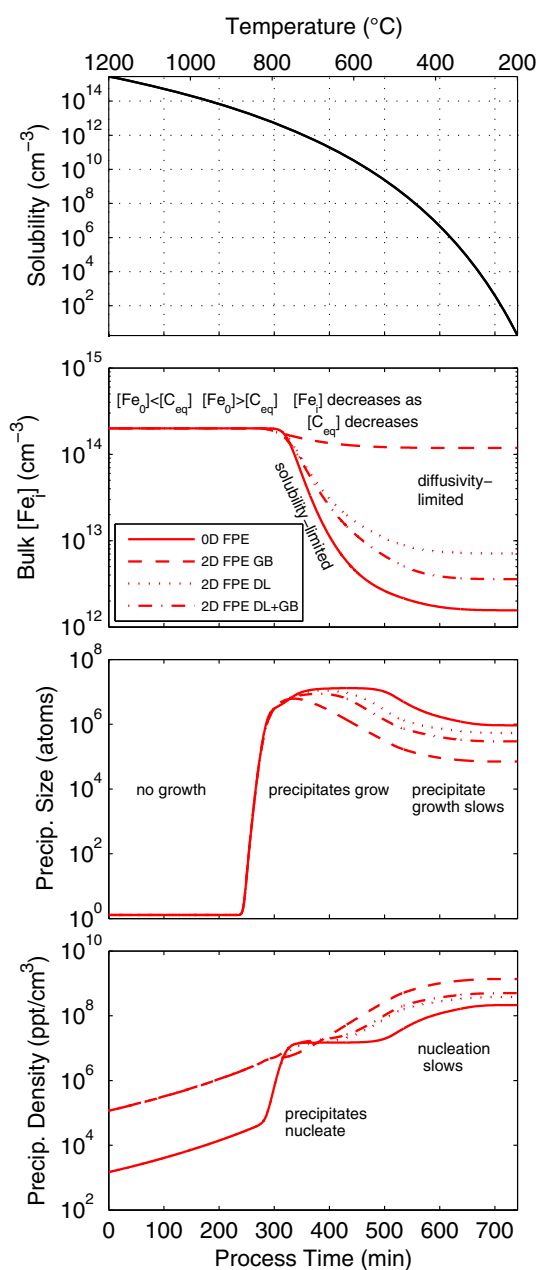


Fig. 4 Temperature and solubility (panel 1), average bulk $[Fe_i]$ (panel 2), average precipitate size (panel 3), and average precipitate density (panel 4) as crystallization proceeds for $[Fe_0] = 2 \times 10^{14} \text{ cm}^{-3}$. Precipitate nucleation and growth occur simultaneously at ~ 250 min. The noticeable increase in precipitate size occurs before the noticeable increase in precipitate density because of the large population of the small unstable precipitates

precipitation is at *Stage I* (see Fig. 2). The iron solid solubility is greater than $[Fe_0]$, so all of the iron is dissolved as Fe_i . The FPE model includes random fluctuations in the precipitate sizes [see $B(n,t)$ in “Appendix 2”], which results in a number of precipitates with sizes that oscillate between small precipitates and full dissolution. Thus, immediately, the average precipitate density is nonzero,

and the average precipitate size remains at ~ 1 Fe atom until ~ 250 min. As the temperature decreases, the solubility decreases exponentially. At ~ 250 – 300 min, the supersaturation of iron point defects is high enough to favor significant precipitate nucleation, and *Stage II* precipitation begins. Precipitates nucleate and grow. Consistent with other systems undergoing phase transition [72], the growth is very rapid at this point. There is a short period of *Stage III* precipitation at ~ 400 min, and then the average size slightly decreases due to the formation of new (small) precipitates and saturates as nucleation and diffusivity drop off at low temperatures. Models with higher average precipitate densities have smaller average precipitate size.

The behavior of these four Models during crystallization can be described by two regimes of iron precipitation: *diffusivity-limited* and *solubility-limited*.

Iron precipitation is *solubility-limited* when the availability of precipitation sites is relatively high and Fe_i can readily reach precipitation sites. $[Fe_i]$ more closely follows the equilibrium iron solubility and is closer to thermodynamic equilibrium. During the crystallization simulated here, the first 500 min of the process can be considered *solubility-limited*. Between 250 and 500 min, $[Fe_i]$ follows a certain level of supersaturation that trends with the exponential decrease in solubility. $[Fe_0]$ plays a more minor role in determining $[Fe_i]$ in the final crystal. This is the case for any Model with dislocations spread throughout the grain, including 0D, 2D FPE DL, and 2D FPE DL+GB. The 2D FPE DL and 2D FPE DL+GB Models predict similar $[Fe_i]$ because the grain boundary has a small internal gettering effect relative to the dislocations in the bulk for the parameters used. The 2D FPE DL+GB $[Fe_i]$ prediction of $3\text{--}4 \times 10^{12} \text{ cm}^{-3}$ is very close to the measured as-grown $[Fe_i]$ values for mc-Si in Hofstetter et al. [73]. The 2D GB case is an extreme case, which we show as a point of reference. Note that the 0D Model predicts the largest reduction in $[Fe_i]$, because precipitation sites are homogeneously distributed throughout the material and are thus, on average, faster to access for Fe_i atoms.

Precipitate growth is *diffusivity-limited* when iron must diffuse either to a limited density of precipitation sites or, on average, to the far-away precipitation sites to precipitate out. The latter is the case of the 2D GB Model because the high density of precipitation sites is located in the few microns at the edge of the grain. In this *diffusivity-limited* regime, $[Fe_0]$ plays a large role in determining the iron distribution after crystallization: First, a higher $[Fe_0]$ results in a higher density of precipitates, which translates into a higher density of Fe_i sinks. Second, if supersaturation (i.e., the onset of precipitation) occurs at higher

temperatures, iron can more easily diffuse to precipitation sites, given the exponential dependence of diffusivity on temperature. Finally, precipitating iron generates a strong Fe_i concentration gradient, creating a “feedback loop” that drives more iron to precipitate; this concentration gradient is stronger with higher $[Fe_0]$. Thus, the effect of higher $[Fe_0]$ is somewhat compensated at the end of crystallization, and $[Fe_0]$ and the precipitation site (i.e., structural defect) distribution together determine the resulting $[Fe_i]$.

All four of the Models are *diffusivity-limited* for the last ~ 200 min of the crystallization because the diffusivity of iron point defects, and thus the addition of iron to grow precipitates, decreases exponentially with temperature. In this last portion of the crystallization, the diffusivity decreases from 5×10^{-8} down to 10×10^{-10} cm²/s. This kinetic limit results in a saturation of the $[Fe_i]$, precipitate size, and precipitate density even though $[Fe_i]$ exceeds the solid solubility during this part of the process.

3.1.2 Heating up to full precipitate dissolution

Ingot crystallization (Sect. 3.1.1) sets the initial wafer conditions and highlights the effect of the differences between the four structural defect distributions. In this section, we explore the effect of a heating step after crystallization or wafering, as has been proposed to maximize gettering efficiency in a subsequent phosphorus diffusion step [17, 26, 67, 74]. The analysis also applies for any thermal step that can be performed in the absence of a phosphorus-rich surface layer. To initialize the Ham’s law Models, we use the post-crystallization average precipitate size and spatial density from the FPE Models. When calculating the average precipitate density for Ham’s law, we counted only precipitates $>10^4$ atoms to exclude the very small, but unstable, precipitates that are present due to the random fluctuations of precipitate size in the FPE Models. Thus, we can analyze the iron distribution during heating for all eight Models described in Sect. 2. We simulate heating from 500°C to 1150°C at 0.75 °C/min to examine a wide range of temperatures up through full precipitate dissolution. The temperature, solubility, average $[Fe_i]$, average precipitate size, and average precipitate density as a function of time during heating for $[Fe_0] = 2 \times 10^{14}$ cm⁻³ are shown in Fig. 5. See Online Resource 3 for the evolution of temperature, solubility, and diffusivity as a function of time during heating. Results for both $[Fe_0]$ values are in Online Resource 4.

For all eight Models, the evolution of $[Fe_i]$ has two phases. Early in the heating process, $[Fe_i]$ is supersaturated, so iron diffuses to precipitates, and precipitates grow. Fe_i is in a *diffusivity-limited* regime, so the precise time at which

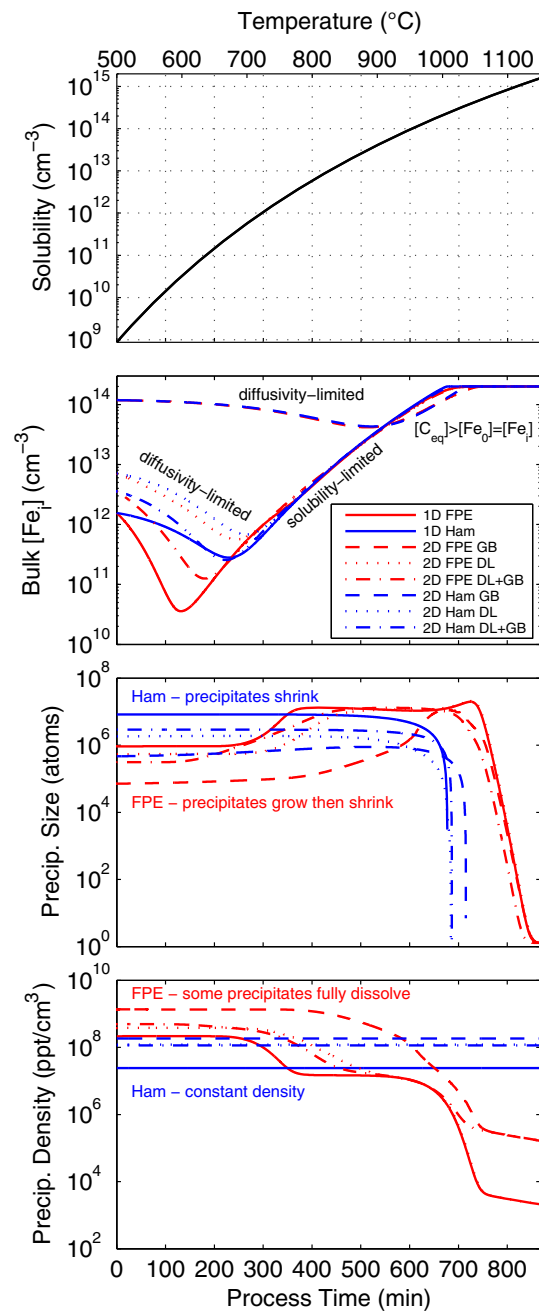


Fig. 5 Temperature and solubility (panel 1), average bulk $[Fe_i]$ (panel 2), average precipitate size (panel 3), and average precipitate density (panel 4) during heating linearly from 500 to 1150 °C for $[Fe_0] = 2 \times 10^{14}$ cm⁻³

the minimum in $[Fe_i]$ occurs depends on the precipitation site distribution, the set of precipitation equations, and the heating rate. The significant initial change in $[Fe_i]$ is accompanied with a barely visible change in average precipitate size and density due to the much higher amount of precipitated iron present. For the 2D GB Models, the minimum in $[Fe_i]$ occurs much later than the other Models because the high concentration of precipitates within a

small volume of material creates a kinetic limitation, as iron dissolving from precipitates must first diffuse into the grain before the next layer of iron can dissolve. Next, at higher temperatures after the minimum in $[\text{Fe}_i]$, the Models enter a more *solubility-limited* regime. Precipitates begin to dissolve, and $[\text{Fe}_i]$ increases uniformly in all Models with most curves overlapping. All eight Models eventually reach the same state in which the solid solubility exceeds the $[\text{Fe}_0]$, so the average $[\text{Fe}_i] = [\text{Fe}_0]$ with precipitates fully dissolved.

The precipitate evolution depends strongly on the precipitation Model. The Ham's law and FPE precipitation Model Elements treat the precipitate size and precipitate density oppositely; however, they result in similar $[\text{Fe}_i]$ predictions. With the FPE Models, during the first 600 min, the average precipitate size increases slightly as small precipitates dissolve, reflected in a slight drop of average precipitate density. Then, the precipitate size rapidly decreases as the remaining precipitates dissolve. For Ham's law, there is a slow decrease in average precipitate size because no density change is allowed. Instead, the singular precipitate size decreases negligibly, followed by a precipitous drop as the solubility exceeds the total iron concentration, driving rapid dissolution. For FPE, the precipitate densities decrease monotonically with a similar *S*-shape as temperature increases, indicating no significant new nucleation at low temperatures and (near) full dissolution at high temperatures. For Ham's law, the precipitate density stays at the predetermined value, eventually exceeding the density predicted by the FPE Models.

Cooling is an inherent component of solar cell manufacturing processes, and the precise time-temperature profiles are essential for controlling the post-processing iron distribution and solar cell performance [18, 73, 75]. For iron evolution during cooling at $10^\circ\text{C}/\text{min}$ from 1150 to 500°C after the heating step discussed in this section, see Online Resource 5. The trends of cooling are essentially the reverse of heating, with differences due to the different nucleation behavior and also depending on how *diffusivity*- or *solubility-limited* the impurity and structural defect distributions are. The Ham's law scenarios predict the onset of $[\text{Fe}_i]$ reduction before the FPE Models because they do not assume a nucleation barrier, so the precipitates with their predetermined density can start to grow immediately. For the FPE Models, there is a slight decrease in average precipitate size during the lower temperatures due to the dominance of new nucleation over growth of existing precipitates. The cooling rates used in solar cell processing are typically faster than the solubility-limited $1.35^\circ\text{C}/\text{min}$ of crystallization, and they can range from $3^\circ\text{C}/\text{min}$ during cooling after phosphorus diffusion up to $100^\circ\text{C}/\text{min}$ or more during contact

metallization firing. In these faster cooling scenarios, iron behavior is much more *diffusivity-limited* and the Model predictions differ more strongly, so the choice of Model is more important.

3.2 Phosphorus diffusion gettering and contact firing: processes with a phosphorus-rich boundary layer

In typical diffused-junction *p*-type Si solar cells, phosphorus diffusion serves two purposes: *p*-*n* junction formation and impurity gettering. In *n*-type Si devices, phosphorus can be used to getter impurities [36, 38, 76–78] and to form a front (or rear) surface field layer [79, 80]. Process Simulations are often used to optimize phosphorus diffusion gettering parameters, and the final spatial and chemical impurity distribution determine minority carrier lifetime, so it is essential to understand what the different Models predict under different processing conditions and different material qualities. See [19, 27, 29, 74, 81–83] for further details about impurity evolution during phosphorus diffusion gettering. The initial conditions are set by the state at the end of the crystallization process described in Sect. 3.1.1. The average precipitate density and size for the Ham's law Models are calculated based on the output of the FPE Models after the crystallization step as in Sect. 3.1.2.

3.2.1 Phosphorus diffusion gettering (PDG) at different plateau temperatures

The phosphorus diffusion plateau temperature is chosen carefully because the junction depth and impurity kinetics and thermodynamics depend exponentially on temperature. Consistent with previous work [67], we simulate phosphorus diffusion with a three-part time-temperature profile shown in Fig. 6: heat linearly from 800°C to the diffusion

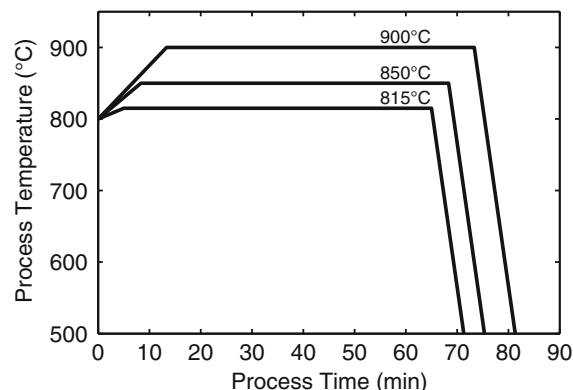


Fig. 6 Phosphorus diffusion gettering profiles with different 60-min plateau temperatures

temperature, hold at the in-diffusion temperature for 60 min, then cool linearly to 500 °C at 50 °C/min. We simulated three different in-diffusion temperatures of 815, 850, and 900 °C, resulting in a wide range of phosphorus profiles suitable for different solar cell architectures. We assume a fixed surface phosphorus concentration of $4.1 \times 10^{20} \text{ cm}^{-3}$. We simulated initial total iron concentrations of $[\text{Fe}_0] = 3.5 \times 10^{13} \text{ cm}^{-3}$ and $2 \times 10^{14} \text{ cm}^{-3}$. In Fig. 7, we show iron evolution during the two extreme cases of high temperature (900 °C) for low $[\text{Fe}_0]$ ($3.5 \times 10^{13} \text{ cm}^{-3}$) and low temperature (815 °C) for high $[\text{Fe}_0]$ ($2 \times 10^{14} \text{ cm}^{-3}$). The rest of the iron distributions as a function of time for 815 and 900 °C are shown in Online Resource 6. The trends for 850 °C are in between those of the other two temperatures.

For all Models and phosphorus diffusion scenarios, the evolution of the iron distribution follows three phases, corresponding to the three parts of the phosphorus diffusion step (separated by vertical gray lines in Fig. 7). First, $[\text{Fe}_i]$ is *solubility-limited* as the wafer is heated from 800 °C to the in-diffusion temperature. With the exception of the 2D GB Models, the solid solubility exceeds $[\text{Fe}_i]$, dissolving precipitates and increasing $[\text{Fe}_i]$. Next, as the wafer is held at the diffusion temperature and phosphorus is introduced, iron behavior can be either *solubility-* or *diffusivity-limited*. During phosphorus diffusion, precipitates are sources of Fe_i and the phosphorus-rich layer is a sink for Fe_i . $[\text{Fe}_0]$ and the phosphorus in-diffusion temperature together determine the balance between precipitate dissolution, which increases bulk $[\text{Fe}_i]$, and external segregation

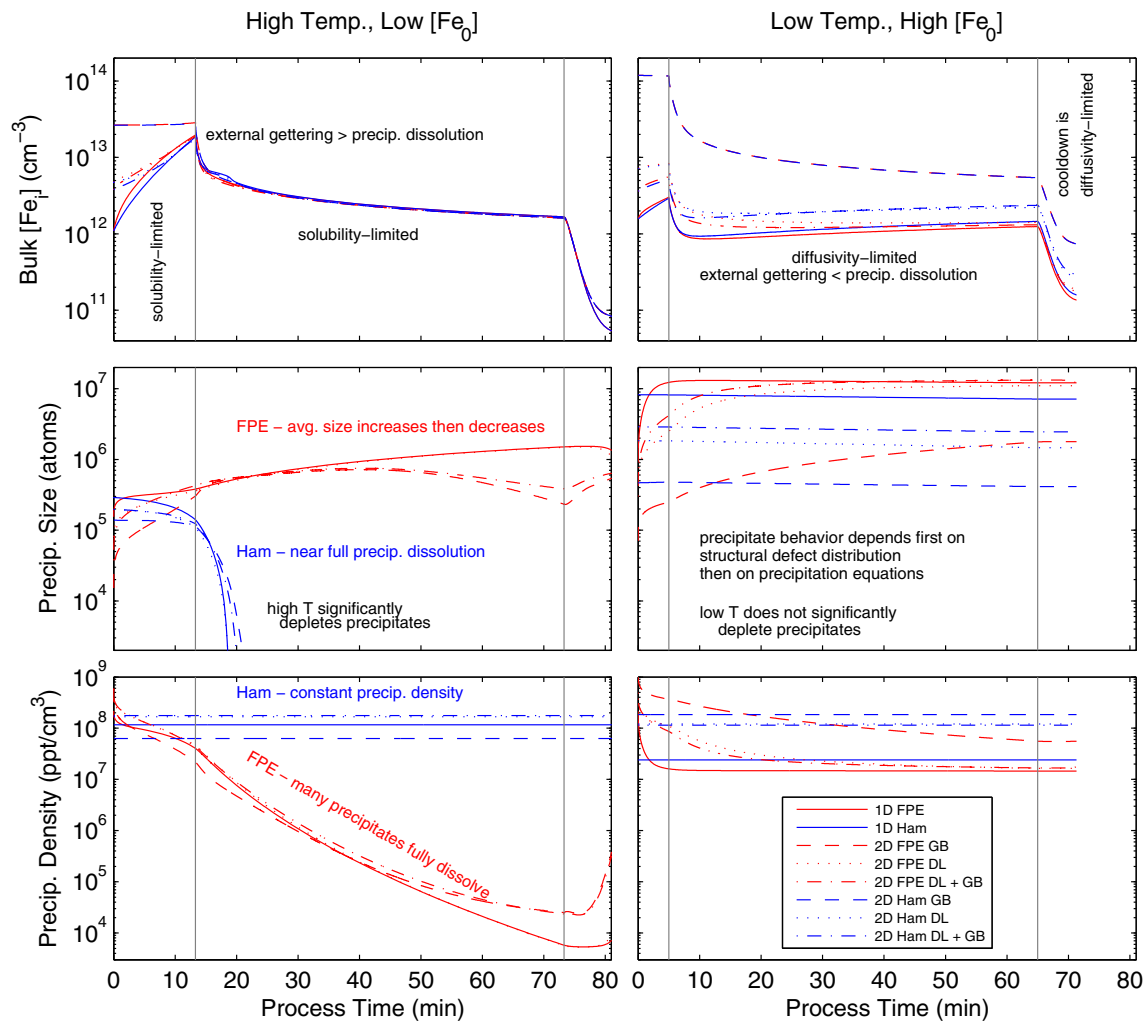


Fig. 7 Average $[\text{Fe}_i]$ (top), precipitate size (middle), and precipitate density (bottom) during phosphorus diffusion gettering at 900 °C for $[\text{Fe}_0] = 3.5 \times 10^{13} \text{ cm}^{-3}$ (left) and at 815 °C for $[\text{Fe}_0] =$

$2 \times 10^{14} \text{ cm}^{-3}$ (right). The vertical gray lines delineate the borders between the three sections of the time-temperature profiles

gettering of point defects, which decreases bulk $[Fe_i]$. The relative rates of these two processes determine the slope of $[Fe_i]$ versus time. Reducing $[Fe_i]$ during this part of phosphorus diffusion requires the process to be mainly *solubility-limited*, meaning that precipitate dissolution must add $[Fe_i]$ to the bulk more slowly than external gettering removes $[Fe_i]$. For low $[Fe_0]$ and high temperature, precipitates, $[Fe_i]$ sources, are significantly depleted, and external gettering can remove the previously precipitated iron. Although the 2D GB Models are *diffusivity-limited*, they have a negative slope because external gettering of the high post-crystallization $[Fe_i]$ levels typically dominates. Finally, in a *diffusivity-limited* process, the wafer is cooled rapidly from the in-diffusion temperature. The decreasing temperature increases the driving force for point defect segregation to the phosphorus-rich region, reducing the bulk $[Fe_i]$. The high supersaturation during cooling can cause some precipitate nucleation as shown in the precipitate density graph for the low $[Fe_0]$ scenario in Fig. 7. The exponentially decreasing diffusivity opposes the increasing segregation force, eventually slowing the Fe_i reduction.

To more easily compare the predicted magnitudes of $[Fe_i]$, the $[Fe_i]$ before and after phosphorus diffusion for all the simulated processes are shown in Online Resource 7. Generally, the most significant factors defining post-phosphorus diffusion $[Fe_i]$ are $[Fe_0]$ [73] and phosphorus diffusion temperature. Overall, the post-gettering $[Fe_i]$ predictions are rather similar. In spite of the wide range of temperatures and Model differences, the range of post-gettering $[Fe_i]$ is only 1.5 orders of magnitude. The largest reduction in $[Fe_i]$ occurs for the 2D GB Models because they start with the highest $[Fe_i]$ post-crystallization. The smallest reduction is for the 1D Models because they start with the lowest $[Fe_i]$. Removal of bulk $[Fe_i]$ in the 2D GB Models is limited only by external gettering and essentially never by precipitate dissolution, whereas the 1D Models are limited by both processes.

For the more *solubility-limited* low $[Fe_0]$, a higher temperature PDG more effectively reduces $[Fe_i]$ because precipitates (finite sources) are more completely dissolved at higher temperature and external gettering is fast enough to remove the resulting point defects. For the more *diffusivity-limited* high $[Fe_0]$, a lower temperature PDG results in lower $[Fe_i]$ because the PDG typically does not dissolve a significant fraction of the precipitates, and external gettering can remove the point defects that do dissolve. As $[Fe_0]$ increases, $[Fe_i]$ depends more strongly on precipitate size and density, so more variation is observed between the different precipitation models. For the high $[Fe_0]$, the 2D GB Models show a decrease in $[Fe_i]$ as temperature increases because they are always *diffusivity-limited*. Longer or even higher temperature gettering may be of interest for materials dominated by precipitated metals at structural defects.

Within each $[Fe_0]$ and for each temperature, the differences in $[Fe_i]$ predictions are most strongly dependent on the structural defect distribution and secondarily dependent on the precipitation model element because $[Fe_i]$ reduction during PDG is typically ultimately limited by diffusion to the emitter, not by precipitate dissolution. The 1D Models and the 2D Models have very similar results. The Ham's law Models predict a higher bulk $[Fe_i]$ because they generally model a higher density of precipitates, which are sources of $[Fe_i]$. However, $[Fe_i]$ predictions are similar for a given $[Fe_0]$, despite significant differences in the precipitate evolution. It is important to note that the uncertainty in the Models themselves is likely greater than the differences between the Models shown here.

Finally, to offer a more complete picture of the behavior of the Models as a function of the initial iron concentration, we simulated the crystallization and the 815 °C PDG process for a range of $[Fe_0]$ values from 10^{12} cm^{-3} to 10^{15} cm^{-3} . The resulting interstitial iron concentrations for $[Fe_0]$ between 10^{13} and 10^{15} cm^{-3} are shown in Fig. 8. For $[Fe_0] < 10^{13} \text{ cm}^{-3}$ the Models are all very similar, and as $[Fe_0]$ decreases, $[Fe_i]$ continues to decrease exponentially. The behavior of the Models falls into three groups:

- (1) 2D FPE GB and 2D Ham GB,
- (2) 2D Ham DL and 2D Ham DL+GB, and
- (3) 1D FPE, 1D Ham, 2D FPE DL and 2D FPE DL+GB.

For $[Fe_0]$ levels below $\sim 4 \times 10^{13} \text{ cm}^{-3}$, the Models are *solubility-limited*, where the residual iron concentration is

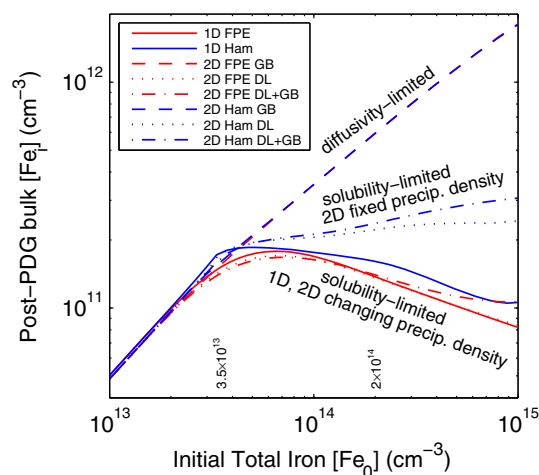


Fig. 8 $[Fe_i]$ after crystallization and PDG at 815 °C as a function of a wide range of $[Fe_0]$ for all eight Models. The Models predict very similar $[Fe_i]$ for $[Fe_0] < \sim 4 \times 10^{13} \text{ cm}^{-3}$. Above $[Fe_0] \sim 4 \times 10^{13} \text{ cm}^{-3}$, the Models fall into three distinct groups. The two $[Fe_0]$ values that we focus on in this work are indicated along the x-axis. The low $[Fe_0]$ is close to where the Models diverge, and the high $[Fe_0]$ is in the regime where there is significant divergence in the Models

mostly determined by the gettering efficiency of the phosphorus emitter. However, after the contamination level considerably surpasses the solid solubility of iron at 815 °C ($\sim 8 \times 10^{12} \text{ cm}^{-3}$), the role of precipitation becomes more important. Further simulations (not shown here) also revealed that with higher PDG temperature, and thus solid solubility, the $[\text{Fe}_0]$ level where the models begin to differ increases.

After the Models deviate, Group 1 is in the *diffusivity-limited* regime, where post-crystallization $[\text{Fe}_i]$ is high because the iron does not have time to diffuse to the grain boundary, and hardly any additional gettering effect is gained from precipitation at structural defects. The exponential increase in final $[\text{Fe}_i]$ as a function of $[\text{Fe}_0]$ observed in Group 1 Models slows slightly at $[\text{Fe}_0]$ levels over $\sim 4 \times 10^{13} \text{ cm}^{-3}$. This is due to the fact that a higher initial iron concentration results in larger precipitates after crystallization, as shown in Fig. 4. When iron is distributed in fewer, but larger precipitates, the dissolution of these precipitates during PDG is slower, which results in a lower $[\text{Fe}_i]$ after PDG. The rest of the Models (Groups 2 and 3) fall into the *solubility-limited* regime, with slight differences in magnitude. With increasing $[\text{Fe}_0]$, Group 2 Models diverge from Group 3 because their precipitate density is fixed, and thus, the precipitate density reduction exhibited in the FPE Models during PDG (evident from Fig. 7) does not occur. This subsequently leads to more iron sources toward the end of PDG for Group 2 Models and results in a slightly larger post-PDG $[\text{Fe}_i]$. It should be noted, however, that the decrease in the final $[\text{Fe}_i]$ as a function $[\text{Fe}_0]$ predicted for the Group 3 Models does not necessarily translate into improved performance of the final solar cell, because of the increased amount of precipitated iron [27].

3.2.2 Different PDG approaches (preanneal peak, standard PDG, annealing)

Variations on the 815 °C standard (PD) time-temperature profile shape discussed in Sect. 3.2.1, including a “preanneal peak” (Peak) and low-temperature anneal (Anneal), have been shown to reduce $[\text{Fe}_i]$ more effectively [26, 67, 84–87]. In Michl et al., four variations of phosphorus diffusion time-temperature profile shape were analyzed. They are the 815 °C reference profile (PD), the reference followed by a post-deposition low-temperature anneal at 600 °C (PD+Anneal), the reference preceded by a pre-deposition 900 °C precipitate dissolution peak (Peak+PD), and finally all three segments together (Peak+PD+Anneal). Compared to the 71-min PD profile, the Anneal adds 248 min and the Peak adds 44 min. The four profiles are reproduced in Online Resource 8. As before, we simulate

initial total iron concentrations of $[\text{Fe}_0] = 3.5 \times 10^{13} \text{ cm}^{-3}$ and $2 \times 10^{14} \text{ cm}^{-3}$. Here, we focus on comparing the predictions from the different Models. The temperature and iron distributions as a function of time for the Peak+PD+Anneal are shown in Fig. 9 with the high $[\text{Fe}_0]$ shown in Online Resource 9. The PD is shown in Fig. 7, and trends for the Peak+PD and the PD+Anneal are a subset of the profiles shown with slight differences in magnitude.

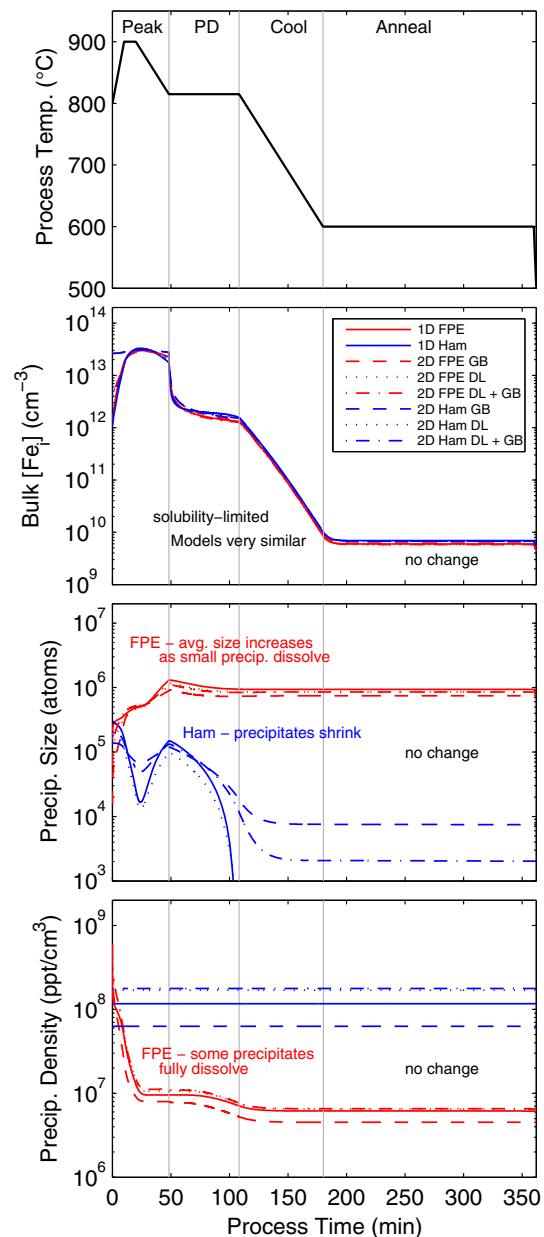


Fig. 9 Temperature (panel 1) and average $[\text{Fe}_i]$ (panel 2), precipitate size (panel 3), and precipitate density (panel 4) during Peak+PD+Anneal phosphorus diffusion gettering $[\text{Fe}_0] = 3.5 \times 10^{13} \text{ cm}^{-3}$. The vertical gray lines delineate the borders between the sections of the time-temperature profile

The preanneal peak step is in the *solubility-limited* regime. During the preanneal peak step, no phosphorus is present, so there is no point defect segregation. As the wafer is heated to and annealed at 900 °C, $[\text{Fe}_i]$ approaches the total iron concentration. As the wafer cools from 900 °C to the phosphorus in-diffusion temperature of 815 °C, the decreasing solubility drives precipitate growth but no significant precipitate nucleation. The main benefit of the preanneal peak is to reduce the precipitated iron concentration by either size or density reduction ahead of the phosphorus diffusion step so that precipitate dissolution does not limit external gettering of point defects. For example, during the 815 °C standard process for $[\text{Fe}_0] = 3.5 \times 10^{13} \text{ cm}^{-3}$ (Online Resource 6), precipitates do not fully dissolve, but during the PD portion of the Peak+PD+Anneal, nearly full dissolution occurs. As discussed before, the phosphorus diffusion step is typically a mix of *solubility-* and *diffusivity-limited* regimes. The Ham's law Models account for a precipitate behavior with a monotonically decreasing precipitate size and a constant precipitate density. On the other hand, the FPE Models account for the behavior with a monotonically decreasing precipitate density and increasing precipitate size. The cooldown from the phosphorus diffusion temperature of 815 °C to the post-deposition annealing temperature of 600 °C at 3 °C/min reduces $[\text{Fe}_i]$ by over two orders of magnitude without significant change in precipitate size or density. The decreasing temperature increases the difference in bulk and emitter solubility, driving Fe_i to the emitter. The transition between phosphorus diffusion temperature and post-deposition anneal is governed by the solubility difference between the bulk and the emitter and is thus *solubility-limited*, and the similar $[\text{Fe}_i]$ at the beginning of the cooldown leads to similar $[\text{Fe}_i]$ Model predictions after the cooldown. For these time-temperature profile parameters, the $[\text{Fe}_i]$ at the beginning of the 600 °C anneal is close to the solid solubility ($\sim 10^{10} \text{ cm}^{-3}$) [40], so no significant change in $[\text{Fe}_i]$ or precipitates is observed during the low-temperature plateau. The relative invariance of the precipitate distribution during a post-PDG anneal has also been observed experimentally [88].

To more easily compare the predicted magnitudes of $[\text{Fe}_i]$, the $[\text{Fe}_i]$ before and after phosphorus diffusion for all the simulated processes are shown in Online Resource 10. For the low $[\text{Fe}_0]$, the Model predictions are nearly identical, while for the high $[\text{Fe}_0]$, there are some differences with the 2D GB Models as the typical outliers. All the profiles reduce $[\text{Fe}_i]$ by over 80 %, with the most important factor being the presence or absence of the slow cooling step associated with the low-temperature anneal. The Peak is predicted to make almost no difference in $[\text{Fe}_i]$ for the low $[\text{Fe}_0]$ and a slight increase in $[\text{Fe}_i]$ for the high $[\text{Fe}_0]$

with the exception of the 2D GB Models. The predictions vary more as $[\text{Fe}_0]$ increases because $[\text{Fe}_i]$ more strongly depends on the precipitate distribution, which is determined by the precipitation site distribution and the precipitation Model Element details as discussed previously.

Although the focus of this paper is on the physical trends of the different Models, we can compare the Model predictions to the limited experimental data available for these exact profiles in [67]. Note that the cooling rate of 50 °C/min from either the PD (if no subsequent anneal) or the Anneal portion was chosen to closely match the experimental data in [67], and the cooling rate has a strong effect on how much time iron has to precipitate and segregate during cooling, thus affecting the final $[\text{Fe}_i]$. The effect is larger if the wafers are pulled out directly after the PD step without the Anneal portion. Excluding the 2D GB Models, which are known to not be representative of the mc-Si used in the study, the PD and Peak+PD simulated and experimental $[\text{Fe}_i]$ are within a factor of two in magnitude. For the high $[\text{Fe}_0] = 2 \times 10^{14} \text{ cm}^{-3}$, the Models in this work predict that the Peak+PD results in a slightly higher post-gettering $[\text{Fe}_i]$ than the PD alone. For both $[\text{Fe}_0]$, the Models overestimate the $[\text{Fe}_i]$ reduction due to the Anneal step by about an order of magnitude. Overall, although there are discrepancies, all of the Models considered here simulate the main trends and magnitudes of post-gettering $[\text{Fe}_i]$ fairly well.

3.2.3 Firing in the presence of a phosphorus-rich layer

In a typical solar cell, using a rapid (<1 min), high-temperature ($\sim 800\text{--}900$ °C) spike, the screen-printed metal pastes are fired through a SiN_x layer to form a good Ohmic contact with the silicon substrate. The exact profile shape depends on the metal paste being used, and here we use a typical profile, which is the same as that used in [67]. We focus on the effect of the thermal step on the iron dynamics in the presence of the phosphorus-rich layer and do not include in our analysis other aspects that may have a secondary effect (such as the potential hydrogenation due to the silicon nitride layer [89] or gettering if an aluminum back surface field is present [90, 91]). We use a no-flux boundary condition for the phosphorus in these firing simulations to describe the fact that there is no additional phosphorus source present at the surface during firing, and we simulate a phosphorus-rich emitter on only one side of the wafer.

For low and high $[\text{Fe}_0]$ and for firing after the four different PDG approaches discussed in Sect. 3.2.2, we simulated the iron distribution as a function of time using all eight Models. The evolution of iron as a function of time during firing for the Peak+PD+Anneal phosphorus

diffusion process for the high $[\text{Fe}_0] = 2 \times 10^{14} \text{ cm}^{-3}$ is shown in Fig. 10. The trends are similar for the other scenarios, and $[\text{Fe}_i]$ before and after firing for all the simulated scenarios are summarized in Online Resource 11.

The rapid temperature change during firing is a strongly *diffusivity-limited* process. The trends in Model predictions of post-phosphorus diffusion gettering $[\text{Fe}_i]$ persist after firing. During firing, the precipitated iron distribution does not undergo major changes, and correspondingly, the

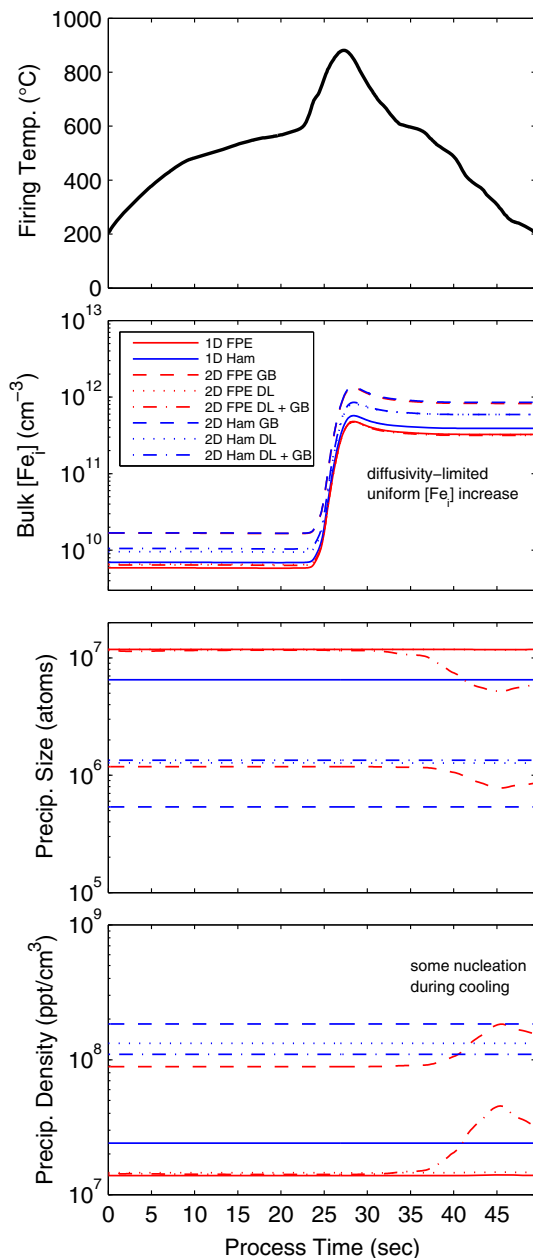


Fig. 10 Evolution of temperature, $[\text{Fe}_i]$, precipitate size, precipitate density during Firing after Peak+PD+Anneal phosphorus diffusion for $[\text{Fe}_0] = 2 \times 10^{14} \text{ cm}^{-3}$

differences between the models are small. However, there is a two orders of magnitude increase in $[\text{Fe}_i]$ when the temperature peaks. In our simulations, the $[\text{Fe}_i]$ increases mostly due to iron out-diffusion from the emitter as observed in [92], with precipitate dissolution also playing a minor role. The out-diffusion is caused by a strong decrease in the segregation coefficient as a function of temperature, which releases iron point defects from the emitter into the bulk. Also, due to the no-flux phosphorus boundary condition, the phosphorus profile diffuses deeper into the bulk and the surface concentration decreases, slightly reducing the total segregation effect. Toward the end of the firing, around 30–45 seconds, some of these released iron point defects precipitate out and a part of the released iron is also gettered back to the emitter. In Fig. 10, the 2D FPE DL+GB and 2D FPE GB Models predict slight precipitate nucleation and thus a decrease in average size during cooling. In the Ham's law Models, this change in precipitates is sometimes seen as a subtle increase in average precipitate size.

It is important to note that the $[\text{Fe}_i]$ reduction due to annealing (as in the PD+Anneal and Peak+PD+Anneal profiles) is almost completely reversed during firing. Thus, the reduction in $[\text{Fe}_i]$ after P-diffusion can be erased [67, 75]. Firing time-temperature profiles with lower peak temperatures and a slower cooling from the peak as suggested in [75] can reduce $[\text{Fe}_i]$. Overall, the simulations match the experimental data in Michl et al. [67] fairly well (excluding the 2D GB Models for the higher $[\text{Fe}_0]$). For the $[\text{Fe}_0] = 3.5 \times 10^{13} \text{ cm}^{-3}$ the Model predictions for the Peak+PD+Anneal are almost exactly the same as the experimental results, while for the other profiles, the Model predictions are slightly lower than the experimental results by no more than a factor of two. For $[\text{Fe}_0] = 2 \times 10^{14} \text{ cm}^{-3}$ the experimental data for the PD and Peak+PD profiles lie within the range predicted by simulation. The experimental data for the profiles with an Anneal are at or above the predicted values (excluding the 2D GB Models) with the Ham's law values being more accurate than the FPE values.

4 Conclusions

Process Simulation has accelerated optimization of semiconductor processing for the last couple of decades, but with many different Models available, it can be difficult to discern the key differences and similarities between the models and the essential physics occurring during processing. To address both of these needs, we combine Model Elements of three existing solar cell Process Simulation tools into one software environment. We combine

four different structural defect distributions and two sets of iron precipitation equations to create eight distinct processing Models, and we analyze how the iron distribution evolves at different stages of device processing: crystal growth, thermal annealing, phosphorus diffusion, and contact metallization firing.

We define a useful classifying framework of *solubility-limited* and *diffusivity-limited* impurity behavior. The slow cooldown of crystallization is *solubility-limited*, and the $[\text{Fe}_i]$ depends strongly on the structural defect distribution. Heating at low and moderate temperatures is *diffusivity-limited* and depends primarily on structural defect distribution and secondarily on precipitation Model differences, while at higher temperatures, it is *solubility-limited* and there are few differences between the Models. Phosphorus diffusion gettering involves both *diffusivity-* and *solubility-limited* aspects, depending on the total iron concentration, time-temperature profile, structural defect distribution, and precipitation models. For the profiles analyzed here, the Model predictions of post-gettering $[\text{Fe}_i]$ were overall quite similar. Finally, the rapid temperature spike of contact metallization firing is a strongly *diffusivity-limited* process that increases $[\text{Fe}_i]$ uniformly across the Models.

The framework defined here can inform the extension of kinetic defect modeling to other impurities in silicon based on their known solubilities and diffusivities in semiconductor materials, including *n*-type silicon. It is expected that at high temperatures, impurity kinetics for *n*- and *p*-type Si are similar because the material becomes intrinsic. Kinetics at lower temperatures may differ because of Fermi-level effects.

This analysis enables the PV industry to better understand how Si materials with different structural defect distributions, including CZ (0D/1D), mono-like and epitaxially grown Si (DL only), standard mc-Si (DL+GB), and high-performance mc-Si (approximated by GB only), respond to processing and therefore what processing is necessary for each of these materials to achieve high-performance devices. The appropriate and necessary simulation Model can also be matched to the material of interest.

A key figure of merit for any Simulation tool is the required computation time. The 0D/1D Models can be orders of magnitude faster than the 2D Models, and the Ham's law Models are typically faster than the FPE Models. This rigorous analysis quantitatively illustrates when the Models are similar, when they are different, and to what degree. When rapid optimization is paramount, the 0D/1D Models may be the most appropriate for defining a small parameter space of interest, while a combination of experiment and 2D modeling may be more appropriate for fine-tuning. The FPE Models are necessary when the precipitate size distribution [93, 94], nucleation, and full dissolution are important factors such as in crystallization. 2D modeling is needed when analyzing inherently multidimensional

phenomena such as lateral diffusion of point defects and the effect of grain size.

This rigorous Model comparison and analysis provides new physical intuition that informs future material, process, and Process Simulation development and enables scientists and engineers to choose the appropriate level of model complexity (simulation run time) based on material characteristics and processing conditions.

Acknowledgments This material is based upon work supported by the National Science Foundation (NSF) and the Department of Energy (DOE) under NSF CA No. EEC-1041895. Authors from Aalto University acknowledge the financial support from Finnish Technology Agency under the project "PASSI" (project No. 2196/31/2011). A. E. Morishige's research visit to Aalto University in 2013 was supported by the Academy of Finland under the project "Low-Cost Photovoltaics." Authors from Fraunhofer ISE acknowledge the financial support by the German Federal Ministry for the Environment, Nature Conservation and Nuclear Safety within the research cluster "SolarWinS" (contract No. 0325270A-H). A. E. Morishige acknowledges Niall Mangan (MIT) for helpful discussions and the financial support of the Department of Defense through the NDSEG fellowship program. H. S. Laine acknowledges the financial support of the Finnish Cultural Foundation through grant No. 00150504. J. Hofstetter acknowledges support by the A. von Humboldt Foundation through a Feodor Lynen Postdoctoral Fellowship. C. del Cañizo acknowledges the support of the Department of Mechanical Engineering at Massachusetts Institute of Technology through the Peabody Visiting Professorship and the Real Colegio Complutense at Harvard University through a RCC Fellowship.

Appendix 1: Simulating iron precipitate nucleation sites

In all eight Models, including those with grain boundaries, iron-silicide precipitates are assumed to nucleate at precipitation sites along dislocations. In the 2D Models, the heterogeneously distributed intra-grain dislocations are in clusters, each of which has a dislocation density $N_{\text{DL}}(x, y) = C \exp(-\frac{1}{2}(\frac{(y-y_0)^2}{L})^3 - \frac{1}{2}(\frac{(x-x_0)^2}{L})^3)$ where C is the peak precipitation site density in the dislocation, parameter $L = 15 \mu\text{m}$ adjusts how fast the dislocation density is reduced from the center of the cluster, and x_0 and y_0 are randomly chosen coordinates that determine the location of the centrum of the dislocation cluster. C is scaled so that the average dislocation density per area is $N_{\text{avg}} = 8 \times 10^3 \text{ cm}^{-2}$ within the grain. Then, the dislocation density of grid points with dislocation density $< 10 \text{ cm}^{-2}$ is set to zero. The grain boundary is modeled as a dense band of dislocations with an areal density of $2 \times 10^8 \text{ cm}^{-2}$. The simulated grain boundary width is $10 \mu\text{m}$, which is unrealistically wide, but it is still less than 1 % of the grain width, and for computational reasons we use this value. Most importantly, this grain boundary width paired with the dislocation density in the grain boundary preserves an accurate number of total dislocations and therefore precipitation sites at the grain boundary [95]. The precipitation

site density, N_{site} , is proportional to the dislocation density, N_{DL} , as in $N_{\text{site}} = 3.3 \times 10^5 \text{ cm}^{-1} \times N_{\text{DL}}$ [26].

Appendix 2: Detailed description of precipitation equations Model Element

Ham's law [39] describes all the precipitates as spheres with a single average number of atoms/precipitate, n_{avg} . The input parameter is the precipitate density, N_p . The time evolution of the precipitated iron concentration, $[\text{Fe}_p]$, depends on $g(n_{\text{avg}})$ and $d(n_{\text{avg}})$, the precipitate size-dependent precipitate growth and dissolution rates, respectively. C_{Fe} is the interstitial iron concentration, and D_{Fe} is the iron diffusivity. r_c is the size-dependent capture radius of the precipitates. The capture radius determines how close to the center of the precipitates the dissolved iron atoms need to be in order to attach to the iron precipitate. The capture radius and local equilibrium iron concentration are defined differently in the two precipitation approaches. For the Ham's law Model, the equilibrium iron concentration, C_{Eq} , is the solid solubility of iron, C_s , as defined in [40]. The precipitates are modeled as spheres with the volume of a unit cell containing a single iron atom in a β -

FeSi_2 precipitate, $V_p = 3.91 \times 10^{23} \text{ cm}^3$. These equations are summarized in the left-hand column of Table 1.

The Fokker–Planck equation-based precipitation Model analyzes precipitates with a distribution of sizes and assigns a different spatial density for each size [25, 96]. The input parameter is the density of precipitation sites, N_{prec} . The density of precipitates with n atoms is $f(n)$, and the total density of precipitates is $N_p = \int_1^{n_{\text{max}}=10^{10}} f(n)dn$, where n_{max} is the maximum precipitate size. The time evolution of the precipitate distribution, $f(n)$, is described by the FPE [25], and it is numerically solved with Cooper and Chang's method [97]. The factor $A(n, t) = g(n, t) - d(n, t)$ is the net growth rate of the precipitates, and the factor $B(n, t) = \frac{1}{2}[g(n, t) + d(n, t)]$ describes random fluctuations in the precipitate size. The boundary conditions, $f(n = n_{\text{max}}, t)$ and $f(n = 1, t)$, are defined in Table 1, $p_1 = 1 \times 10^4$ is a fitting parameter, and $f(n = 0, t)$ is the density of empty precipitation sites. $f(n = 1, t)$ describes which fraction of these sites contains an iron atom, i.e., where nucleation occurs. The Gibbs free energy of a precipitate with n atoms is $\Delta G(n)$ [98], where E_a is an energy parameter that accounts for all changes in surface energy and strain caused by the growth and dissolution of

Table 1 Equations for precipitation behavior Model Element

Ham's law	Fokker–Planck equation
<i>Evolution of precipitated iron over time</i>	Time-dependent density and size distribution $f(n, t)$
Average time-dependent size	$\frac{\partial f(n, t)}{\partial t} = \frac{\partial}{\partial n} [-A(n, t)f(n, t) + B(n, t)\frac{\partial f(n, t)}{\partial n}]$
	$A(n, t) = g(n, t) - d(n, t)$
	$B(n, t) = \frac{1}{2}[g(n, t) + d(n, t)]$
	Boundary conditions
	$f(n = 1, t) = f(0, t)p_1 \exp\left[\frac{-\Delta G(1)}{kT}\right]$
	$f(n = 0, t) = N_{\text{prec}} - \int_1^{n_{\text{max}}} f(n, t) dn$
	$f(n = n_{\text{max}}, t) = 0$
	$\Delta G(n) = -nkT \ln \frac{C_{\text{Fe}}}{C_s} + 2E_a n^{\frac{1}{2}}$
<i>Precipitate growth and dissolution rates</i>	$g(n, t) = 4\pi r_c(n)D_{\text{Fe}}C_{\text{Fe}}$
	$d(n, t) = 4\pi r_c(n)D_{\text{Fe}}C_{\text{Eq}}(n)$
	$C_{\text{Eq}}(n) = C_s \exp\left(\frac{E_a}{kTn^{\frac{1}{2}}}\right)$
	$E_a = \begin{cases} 1.015 \times 10^{-4} \times T + 0.8033 \text{ eV} & \text{if } T < 773\text{K} \\ 6.038 \times 10^{-4} \times T + 0.4150 \text{ eV} & \text{if } T \geq 773\text{K} \end{cases}$
<i>Precipitate shape and size</i>	Flat disk-shaped precipitates with capture radius r_c
Spherical precipitates with capture radius r_c	$r_c(n) = \begin{cases} 15 \text{ nm} + 0.051 \text{ nm} \times n^{\frac{1}{2}} & \text{if } n < 5.42 \times 10^4 \text{ atoms} \\ \frac{\left(\frac{nV_p}{\pi a}\right)^{\frac{1}{2\pi}}}{\ln\left[16\left(\frac{nV_p}{\pi a^3}\right)^{\frac{1}{2}}\right]} & \text{if } n \geq 5.42 \times 10^4 \text{ atoms} \end{cases}$

precipitates. It has been assumed to be independent of n and has been estimated in [99]. Assuming that precipitation is *diffusivity-limited*, the equilibrium concentration in the proximity of a precipitate is the dissolved iron concentration when $\frac{\partial \Delta G}{\partial n} = 0$. The precipitate size-dependent equilibrium iron concentration, C_{Eq} , depends on the solid solubility of iron, C_S , and the factor in the exponential captures the fact that iron has a higher chemical potential in a small cluster than in a large cluster [25]. Precipitates are modeled as flat disks [98] with thickness $a = 20$ nm, and the capture radius of the precipitation site is explicitly accounted for [100]. Due to the inclusion of the size of the precipitation site, the FPE Model predicts higher capture radii at small precipitate sizes, and due to the faster expansion of 2D disks compared to 3D spheres, the growth of the capture radius remains faster at large precipitate sizes. These equations are summarized in the right-hand column of Table 1.

Note that for large precipitate sizes ($n \gg 1$), $C_{\text{Eq}} \approx C_S$ and the two precipitation models predict similar equilibrium concentrations. However, when modeling small precipitates, the models differ. The expression for the Gibbs free energy predicts a temperature- and dissolved iron concentration-dependent critical size n_{crit} , defined as the size that maximizes $\Delta G(n)$. Thermodynamics dictates that precipitates smaller than n_{crit} tend to dissolve, whereas precipitates larger than n_{crit} tend to grow. The energy needed for the precipitates to cross from the dissolution-favoring regime into the growth regime is defined as the nucleation barrier. In the FPE precipitation Model, a certain level of local supersaturation is needed for nucleation to occur; however, in the Ham's law Model, there is no nucleation barrier.

References

1. Synopsys, Inc., Sentaurus Device User Guide pp. 1–1284 (2010)
2. Silvaco, Inc., Atlas User's Manual (2014)
3. D.A. Clugston, P.A. Basore, in *Proceedings of the 26th IEEE PVSC* (Anaheim, 1997), pp. 207–210
4. P.A. Basore, K. Cabanas-Holmen, *IEEE J. Photovolt.* **1**(1), 72 (2011)
5. Y. Liu, D. Heinzel, A. Rockett, in *Proceedings of the 35th IEEE PVSC* (Honolulu, 2010), pp. 1943–1947
6. M. Burgelman, J. Verschraegen, S. Degraeve, P. Nollet, *Prog. Photovolt. Res. Appl.* **12**(23), 143 (2004)
7. G. Coletti, *Prog. Photovolt. Res. Appl.* **21**, 1163 (2013)
8. A.A. Istratov, T. Buonassisi, R.J. McDonald, A.R. Smith, R. Schindler, J.A. Rand, J.P. Kalejs, E.R. Weber, *J. Appl. Phys.* **94**(10), 6552 (2003)
9. G. Zoth, W. Bergholz, *J. Appl. Phys.* **67**(11), 6764 (1990)
10. M.C. Schubert, H. Habenicht, W. Warta, *IEEE J. Photovolt.* **1**(2), 168 (2011)
11. A.A. Istratov, H. Hieslmair, E.R. Weber, *Appl. Phys. A Mater. Sci. Process.* **69**(1), 13 (1999)
12. T. Buonassisi, A.A. Istratov, M.D. Pickett, M. Heuer, J.P. Kalejs, G. Hahn, M.A. Marcus, B. Lai, Z. Cai, S.M. Heald, T.F. Ciszek, R.F. Clark, D.W. Cunningham, A.M. Gabor, R. Jonczyk, S. Narayanan, E. Sauar, E.R. Weber, *Prog. Photovolt. Res. Appl.* **14**(6), 513 (2006)
13. T. Buonassisi, A.A. Istratov, M.D. Pickett, J.P. Rakotoniaina, O. Breitenstein, M.A. Marcus, S.M. Heald, E.R. Weber, *J. Cryst. Growth* **287**(2), 402 (2006)
14. D. Macdonald, A. Cuevas, A. Kinomura, Y. Nakano, L.J. Geerligs, *J. Appl. Phys.* **97**(3), 033523 (2005)
15. T. Buonassisi, A.A. Istratov, M. Heuer, M.A. Marcus, R. Jonczyk, J. Isenberg, B. Lai, Z. Cai, S. Heald, W. Warta, R. Schindler, G. Willeke, E.R. Weber, *J. Appl. Phys.* **97**(7), 074901 (2005)
16. S.A. MacHugo, H. Hieslmair, E.R. Weber, *Appl. Phys. A Mater. Sci. Process.* **64**(2), 127 (1997)
17. J. Tan, D. Macdonald, N. Bennett, D. Kong, A. Cuevas, I. Romijn, *Appl. Phys. Lett.* **91**(4), 043505 (2007)
18. D.P. Fenning, J. Hofstetter, A.E. Morishige, D.M. Powell, A. Zuschlag, G. Hahn, T. Buonassisi, *Adv. Energy Mater.* **4**(13), 1400459 (2014)
19. D.P. Fenning, A.S. Zuschlag, M.I. Bertoni, B. Lai, G. Hahn, T. Buonassisi, *J. Appl. Phys.* **113**(21), 214504 (2013)
20. W. Kwapil, J. Schön, F. Schindler, W. Warta, M.C. Schubert, *IEEE J. Photovolt.* **4**(3), 791 (2014)
21. M. Seibt, H. Hedemann, A.A. Istratov, F. Riedel, A. Sattler, W. Schröter, *Phys. Status Solidi (A)* **171**, 301 (1999)
22. C. del Cañizo, A. Luque, *J. Electrochem. Soc.* **147**(7), 2685 (2000)
23. H. Hieslmair, S. Balasubramanian, A.A. Istratov, E.R. Weber, *Semicond. Sci. Technol.* **16**(7), 567 (2001)
24. A.L. Smith, K. Wada, L.C. Kimerling, *J. Electrochem. Soc.* **147**(3), 1154 (2000)
25. A. Haarahiltunen, H. Savin, M. Yli-Koski, H. Talvitie, M.I. Asghar, J. Sinkkonen, *Mater. Sci. Eng. B* **159–160**, 248 (2009)
26. J. Schön, H. Habenicht, M.C. Schubert, W. Warta, *J. Appl. Phys.* **109**(6), 063717 (2011)
27. J. Hofstetter, D.P. Fenning, M.I. Bertoni, J.F. Lelièvre, Cd Cañizo, T. Buonassisi, *Prog. Photovolt. Res. Appl.* **19**(4), 487 (2011)
28. R. Chen, B. Trzynadlowski, S.T. Dunham, *J. Appl. Phys.* **115**(5), 054906 (2014)
29. A.A. Istratov, H. Hieslmair, E.R. Weber, *Appl. Phys. A Mater. Sci. Process.* **70**(5), 489 (2000)
30. D. Macdonald, L.J. Geerligs, *Appl. Phys. Lett.* **85**(18), 4061 (2004)
31. J. Schmidt, B. Lim, D. Walter, K. Bothe, S. Gatz, T. Dullweber, P.P. Altermatt, *IEEE J. Photovolt.* **3**(1), 114 (2013)
32. M. Kittler, J. Lärz, W. Seifert, M. Seibt, W. Schröter, *Appl. Phys. Lett.* **58**(9), 911 (1991)
33. Y. Yoon, B. Paudyal, J. Kim, Y.W. Ok, P. Kulshreshtha, S. Johnston, G. Rozgonyi, *J. Appl. Phys.* **111**(3), 033702 (2012)
34. S. Martinuzzi, O. Palais, S. Ostapenko, *Mater. Sci. Semicond. Process.* **9**(1–3), 230 (2006)
35. M. Kittler, W. Seifert, K. Knobloch, *Microelectron. Eng.* **66**(1–4), 281 (2003)
36. A. Cuevas, S. Riepe, M.J. Kerr, D.H. Macdonald, G. Coletti, F. Ferrazza, in *Photovoltaic Energy Conversion, 2003. Proceedings of 3rd World Conference on* (2003), pp. 1312–1315
37. L.J. Geerligs, Y. Komatsu, I. Röber, K. Wambach, I. Yamaga, T. Saitoh, *J. Appl. Phys.* **102**(9), 093702 (2007)
38. A.E. Morishige, D.P. Fenning, J. Hofstetter, M. Ann Jensen, S. Ramanathan, C. Wang, B. Lai, T. Buonassisi, in *Proceedings of the 40th IEEE PVSC* (Denver, 2014), pp. 3004–3007
39. F.S. Ham, *J. Phys. Chem. Solids* **6**(4), 335 (1958)
40. M. Aoki, A. Hara, A. Ohsawa, *J. Appl. Phys.* **72**(3), 895 (1992)

41. M. Seibt, D. Abdelbarey, V. Kveder, C. Rudolf, P. Saring, L. Stolze, O. Voß, Mater. Sci. Eng. B **159–160**, 264 (2009)
42. H. Hieslmair, A.A. Istratov, T. Heiser, E.R. Weber, J. Appl. Phys. **84**(2), 713 (1998)
43. J.D. Murphy, R.J. Falster, J. Appl. Phys. **112**(11), 113506 (2012)
44. A. Bentzen, A. Holt, J.S. Christensen, B.G. Svensson, J. Appl. Phys. **99**(6), 064502 (2006)
45. T.Y. Tan, P.S. Plekhanov, S. Joshi, R. Gafiteanu, U.M. Gösele, in *Eighth Workshop on Crystalline Silicon Solar Cell Materials and Process* (Copper Mountain, 1998), pp. 42–49
46. H.M. You, U.M. Gösele, T.Y. Tan, J. Appl. Phys. **74**(4), 2461 (1993)
47. A. Haarahiltunen, H. Savin, M. Yli-Koski, H. Talvitie, J. Sinkkonen, J. Appl. Phys. **105**(2), 023510 (2009)
48. P. Zhang, H. Väinölä, A.A. Istratov, E.R. Weber, Phys. B Condens. Matter **340–342**, 1051 (2003)
49. K. Hartman, M. Bertoni, J. Serdy, T. Buonassisi, Appl. Phys. Lett. **93**(12), 122108 (2008)
50. D. McDonald, A. Cuevas, *16th European Photovoltaic Solar Energy Conference* (2000)
51. D. Franke, in *Photovoltaic Energy Conversion, 2003. Proceedings of 3rd World Conference on* (2003), pp. 1344–1347
52. B. Wu, N. Stoddard, R. Ma, R. Clark, J. Cryst. Growth **310**(7–9), 2178 (2008)
53. A. Jouini, D. Ponthenier, H. Lignier, N. Enjalbert, B. Marie, B. Drevet, E. Pihan, C. Cayron, T. Lafford, D. Camel, Prog. Photovolt. Res. Appl. **20**(6), 735 (2011)
54. T. Ervik, G. Stokkan, T. Buonassisi, Ø. Mjøs, O. Lohne, Acta Mater. **67**(C), 199 (2014)
55. M.G. Tsoutsouva, V.A. Oliveira, D. Camel, T.N.T. Thi, J. Baruchel, B. Marie, T.A. Lafford, J. Cryst. Growth **401**(C), 397 (2014)
56. L. Gong, F. Wang, Q. Cai, D. You, B. Dai, Solar Energy Mater. Solar Cells **120**(PA), 289 (2014)
57. I. Guerrero, V. Parra, T. Carballo, A. Black, M. Miranda, D. Cancillo, B. Moralejo, J. Jiménez, J.F. Lelièvre, C. del Cañizo, Prog. Photovolt. Res. Appl. **22**(8), 923 (2012)
58. K.M. Han, H. Lee, J.S. Cho, S.H. Park, J.H. Yun, K.H. Yoon, J.S. Yoo, J. Korean Phys. Soc. **61**(8), 1279 (2012)
59. X. Gu, X. Yu, K. Guo, L. Chen, D. Wang, D. Yang, Solar Energy Mater. Solar Cells **101**(C), 95 (2012)
60. R.B. Bergmann, Appl. Phys. A **69**(2), 187 (1999)
61. D.M. Powell, J. Hofstetter, D.P. Fenning, R. Hao, T.S. Ravi, T. Buonassisi, Appl. Phys. Lett. **103**(26), 263902 (2013)
62. M. Keller, S. Reber, N. Schillinger, D. Pocza, M. Arnold, J. Nanosci. Nanotechnol. **11**(9), 8024 (2011)
63. H.M. Branz, C.W. Teplin, M.J. Romero, I.T. Martin, Q. Wang, K. Alberi, D.L. Young, P. Stradins, Thin Solid Films **519**(14), 4545 (2011)
64. Y.M. Yang, A. Yu, B. Hsu, W.C. Hsu, A. Yang, C.W. Lan, Prog. Photovolt. Res. Appl. **23**(3), 340 (2013)
65. G. Hahn, A. Schönecker, J. Phys. Condens. Matter **16**(50), R1615 (2004)
66. A. Schönecker, L.J. Geerligs, A. Müller, Solid State Phenom. **95–96**, 149 (2004)
67. B. Michl, J. Schön, W. Warta, M.C. Schubert, IEEE J. Photovolt. **3**(2), 635 (2013)
68. S.A. McHugo, A.C. Thompson, G. Lamble, C. Flink, E.R. Weber, Phys. B Condens. Matter **273–274**, 371 (1999)
69. A. Bentzen, A. Holt, R. Kopecek, G. Stokkan, J.S. Christensen, B.G. Svensson, J. Appl. Phys. **99**(9), 093509 (2006)
70. D. Macdonald, J. Tan, T. Trupke, J. Appl. Phys. **103**(7), 073710 (2008)
71. S. Riepe, I.E. Reis, W. Kwapil, M.A. Falkenberg, J. Schön, H. Behnken, J. Bauer, D. Kreßner-Kiel, W. Seifert, W. Koch, Phys. Status Solidi (C) **8**(3), 733 (2010)
72. M. M’Hamdi, Thermo-mechanical analysis of multicrystalline silicon ingot casting. Tech. rep. (2007)
73. J. Hofstetter, D.P. Fenning, D.M. Powell, A.E. Morishige, H. Wagner, T. Buonassisi, IEEE J. Photovolt. **4**(6), 1421 (2014)
74. J. Hofstetter, D.P. Fenning, J.F. Lelièvre, C. del Cañizo, Phys. Status Solidi (A) **209**(10), 1861 (2012)
75. J.F. Lelièvre, J. Hofstetter, A. Peral, I. Hoces, F. Recart, C. del Cañizo, Energy Proc. **8**, 257 (2011)
76. G. Coletti, R. Kvande, V.D. Mihailitchi, L.J. Geerligs, L. Arnberg, E.J. Ovreliid, J. Appl. Phys. **104**(10), 104913 (2008)
77. V. Vähänissi, M. Yli-Koski, A. Haarahiltunen, H. Talvitie, Y. Bao, H. Savin, Solar Energy Mater. Solar Cells **114**(C), 54 (2013)
78. M. Kivambe, D.M. Powell, S. Castellanos, M.A. Jensen, A.E. Morishige, K. Nakajima, K. Morishita, R. Murai, T. Buonassisi, J. Cryst. Growth **407**(C), 31 (2014)
79. Y. Tao, Y.W. Ok, F. Zimbardi, A.D. Upadhyaya, J.H. Lai, S. Ning, V.D. Upadhyaya, A. Rohatgi, IEEE J. Photovolt. **4**(1), 58 (2014)
80. P. Rothhardt, S. Meier, S. Maier, K. Jiang, A. Wolf, D. Biro, IEEE J. Photovolt. **4**(3), 827 (2014)
81. A. Luque, S. Hegedus, *Handbook of Photovoltaic Science and Engineering* (Wiley, Hoboken, 2011)
82. D.P. Fenning, J. Hofstetter, M.I. Bertoni, G. Coletti, B. Lai, C. del Cañizo, T. Buonassisi, J. Appl. Phys. **113**(4), 044521 (2013)
83. K. Graf, *Metal Impurities in Silicon-Device Fabrication* (Springer, Berlin, 2012)
84. M.B. Shabani, T. Yamashita, E. Morita, Solid State Phenom. **131**, 399 (2008)
85. M.D. Pickett, T. Buonassisi, Appl. Phys. Lett. **92**(12), 122103 (2008)
86. M. Rinio, A. Yodyunyong, S. Keipert-Colberg, Y.P.B. Mouafi, D. Borchert, A. Montesdeoca-Santana, Prog. Photovolt. Res. Appl. **19**(2), 165 (2010)
87. R. Krain, S. Herlufsen, J. Schmidt, Appl. Phys. Lett. **93**(15), 152108 (2008)
88. D.P. Fenning, J. Hofstetter, M.I. Bertoni, S. Hudelson, M. Rinio, J.F. Lelièvre, B. Lai, C. del Cañizo, T. Buonassisi, Appl. Phys. Lett. **98**(16), 162103 (2011)
89. S. Martinuzzi, Solar Energy Mater. Solar Cells **80**(3), 343 (2003)
90. D. Abdelbarey, V. Kveder, W. Schröter, M. Seibt, Appl. Phys. Lett. **94**(6), 061912 (2009)
91. M. Loghmarti, R. Stuck, J.C. Muller, D. Sayah, P. Siffert, Appl. Phys. Lett. **62**(9), 979 (1993)
92. D. Macdonald, A. Cheung, A. Cuevas, in *Photovoltaic Energy Conversion, 2003. Proceedings of 3rd World Conference on* (2003), pp. 1336–1339
93. V. Vähänissi, A. Haarahiltunen, M. Yli-Koski, H. Savin, IEEE J. Photovolt. **4**(1), 142 (2014)
94. D.P. Fenning, V. Vähänissi, J. Hofstetter, A.E. Morishige, H.S. Laine, A. Haarahiltunen, S. Castellanos, M.A. Jensen, B. Lai, H. Savin, in *Proceedings of the 40th IEEE PVSC* (Denver, 2014)
95. J. Schön, A. Haarahiltunen, H. Savin, D.P. Fenning, T. Buonassisi, W. Warta, M.C. Schubert, IEEE J. Photovolt. **3**(1), 131 (2013)
96. M.C. Schubert, J. Schön, B. Michl, A. Abdollahinia, W. Warta, in *Proceedings of the 38th IEEE PVSC* (Austin, 2012), pp. 286–291
97. J.S. Chang, G. Cooper, J. Comput. Phys. **6**(1), 1 (1970)
98. S.T. Dunham, Appl. Phys. Lett. **63**(4), 464 (1993)
99. A. Haarahiltunen, H. Väinölä, O. Anttila, M. Yli-Koski, J. Sinkkonen, J. Appl. Phys. **101**(4), 043507 (2007)
100. A. Haarahiltunen, H. Talvitie, H. Savin, O. Anttila, M. Yli-Koski, M.I. Asghar, J. Sinkkonen, J. Mater. Sci. Mater. Electron. **19**(S1), 41 (2008)